Role of connectivity and fluctuations in the nucleation of calcium waves in cardiac cells

Gonzalo Hernandez-Hernandez,[1] Enric Alvarez-Lacalle,[2] and Yohannes Shiferaw[1]
[1]*Department of Physics & Astronomy, California State University, Northridge, 18111 Nordhoff Street, Northridge, CA 91330, USA*
[2]*Physics Department, Universitat Politècnica de Catalunya, BarcelonaTech, Barcelona, Spain*
(Received 15 August 2015; published 20 November 2015; corrected 1 December 2015)

Spontaneous calcium release (SCR) occurs when ion channel fluctuations lead to the nucleation of calcium waves in cardiac cells. This phenomenon is important since it has been implicated as a cause of various cardiac arrhythmias. However, to date, it is not understood what determines the timing and location of spontaneous calcium waves within cells. Here, we analyze a simplified model of SCR in which calcium release is modeled as a stochastic processes on a two-dimensional network of randomly distributed sites. Using this model we identify the essential parameters describing the system and compute the phase diagram. In particular, we identify a critical line which separates pinned and propagating fronts, and show that above this line wave nucleation is governed by fluctuations and the spatial connectivity of calcium release units. Using a mean-field analysis we show that the sites of wave nucleation are predicted by localized eigenvectors of a matrix representing the network connectivity of release sites. This result provides insight on the interplay between connectivity and fluctuations in the genesis of SCR in cardiac myocytes.

DOI: 10.1103/PhysRevE.92.052715 PACS number(s): 87.16.A−, 87.19.Hh, 87.10.Mn

I. INTRODUCTION

Calcium (Ca) is a ubiquitous secondary messenger that is responsible for a vast array of subcellular signaling processes such as muscle contraction, cell proliferation, and gene transcription [1]. Ca plays a particularly important role in the cardiac cell as it mediates the coupling between membrane voltage and tissue contraction [2]. A central role in Ca regulation is played by the ryanodine receptor (RyR) which controls the flow of Ca from intracellular Ca stores to the cell interior. An important feature of RyR channels is that they are highly sensitive to Ca and transition from a closed to open state in a Ca-dependent manner. This Ca sensitivity, which is mediated by multiple binding sites on the channel, is further amplified by the close arrangement of RyR channels into clusters of 10–100 RyR channels [2]. This architecture ensures that small increases of local Ca concentration can trigger a domino like opening of an array of RyR channels, leading to a large local release of Ca [3]. In a cardiac cell there are several thousand of these clusters organized along equally spaced planes (Z planes), so that signaling is determined by the number and timing of these release events. This signaling architecture is found in a wide variety of cell types and is utilized to control the spatiotemporal distribution of Ca in the cell [1].

The nonlinear response of RyR receptors in clusters endows the Ca cycling system with the properties of an excitable medium. This is because Ca released at a given cluster can diffuse and activate its nearest neighbors. Thus, under certain conditions a fire-diffuse-fire wave can propagate in the cell [4–6]. These Ca propagation events are referred to as spontaneous Ca release (SCR) since the release that occurs in this fashion is typically initiated by a random opening of a single or group of RyR clusters [4]. These spontaneous Ca waves play an important role in the genesis of cardiac arrhythmias since they can lead to membrane depolarization, which, if it occurs in a population of cells, can induce a focal excitation that propagates in heart tissue [7–9]. These excitations are dangerous because their timing is random and they can therefore disrupt the regular beating of the heart and initiate cardiac arrhythmias [8,10,11]. Despite a great deal of work the basic features of spontaneous Ca waves (SCR) are still not fully understood. Experimental and theoretical studies reveal a wide range of complex spatiotemporal dynamics of Ca depending upon physiological conditions and cell type [12–16]. In particular Bar *et al.* [12] studied stochastic spreading in an array of discrete sites and identified a nonpropagating to propagating transition. Interestingly, the propagation dynamics could be described as a directed percolation process, and also as a depinning transition depending upon the system parameters. More recently, Nivala *et al.* [15] performed numerical and experimental studies to explore the emergence of SCR as a function of sarcoplasmic reticulum (SR) load. These authors found that at low SR loads Ca sparks typically occur in the cell in a stochastic manner but rarely transition to Ca waves. However, as the SR load is increased Ca waves are nucleated in the cell interior with greater frequency; although the distance of propagation is small, i.e., the waves tend to fail after propagating a distance of several micrometers. Further increases in SR load led to longer propagation distances until waves propagate the extent of the cell leading to a substantial release of Ca. In earlier work Marchant and Parker [17] used fluorescence imaging to analyze the nucleation of Ca waves in *Xenopus* oocytes. In these cells Ca release is governed by clusters of inositol (1,4,5)-triphosphate (IP_3) receptors which mediate the flow of Ca in similar fashion as do RyRs in cardiac cells. They found that waves tend to nucleate at specific regions of the cell characterized by a higher density of release sites and sensitivity to stimulation. Furthermore, they noticed that when the period between Ca waves was long then wave nucleation occurred at specific sites with greater reliability. While these studies shed light on various aspects of subcellular Ca dynamics, several questions remain unanswered. For example, it is not known how the spatial distribution of calcium release units (CRUs) combines with fluctuations and excitability to determine the location of wave nucleation sites in the cell.

In this paper we explore a simplified theoretical model that can be used to understand essential features of Ca wave nucleation and propagation. We analyze in detail the role of

 ©2015 American Physical Society

the random arrangement of CRUs inside the cell, the strength of diffusive coupling, and the kinetics of spark activation and extinguishing. Our goal is to determine how these properties determine the location and timing of spontaneous Ca waves in cardiac cells. Using this approach, we show that the dynamics of SCR is crucially dependent on two important parameters. The first is the ratio of the length scale over which Ca diffuses from a Ca spark to the average distance between release sites in the cell, which gives a measure of the degree of coupling between CRUs in a cell. The second parameter is the amount of Ca released during a Ca spark, which determines the excitability of the system. We find that for large excitability, fluctuations play the leading role in the spatiotemporal dynamics of the system. In this regime Ca waves are nucleated randomly in the system, and the spatial arrangement of release sites does not determine the sites of wave nucleation. However, as the excitability is reduced it is the spatial arrangement of Ca release sites which dictates the location of wave nucleation. More precisely, we show that the sites of wave nucleation are determined by eigenvectors of the network connectivity matrix, which represents the strength of diffusive coupling between CRUs. Using a mean-field theory we argue that the initiation of SCR can be viewed as a barrier escape process, which favors wave nucleation at the sites of eigenvector localization. These results help explain several key experimental observations of Ca wave nucleation in biological cells [17]. In particular, they give a quantitative approach to identify sites that are prone to initiate Ca waves, and explain why wave nucleation occurs at these sites, with higher likelihood, as the system excitability is reduced.

II. THE MODEL

A. Biophysical background

In Fig. 1 we illustrate the basic architecture of subcellular Ca signaling in cardiac cells. Here, RyR channels form clusters of 10–150 channels which are distributed in the cell along planar invaginations referred to as Z planes. In this study we will refer to each of these clusters as a Ca release unit. Along each Z plane the distribution of CRUs is random with an average spacing in the range 100–500 nm while the spacing between planes is in the range 1–2 μm [18,19], so that there are roughly 100 CRUs on a Z plane and about 10^4 in the cell. Under normal conditions RyR channels are stimulated by the opening

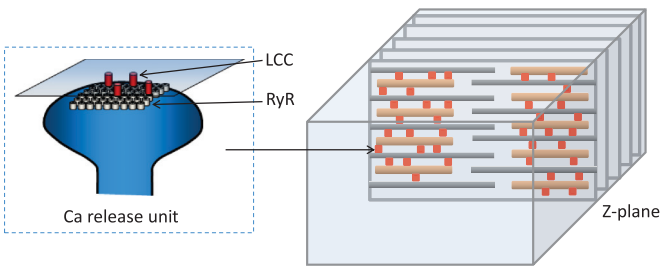

FIG. 1. (Color online) Illustration of the Ca signaling architecture. CRUs contain a few (1–5) LCC channels and a cluster (10–150) of RyR channels responsible for Ca signaling. In ventricular myocytes CRUs are distributed along roughly 50–100 Z planes with ~100 CRUs within each plane.

of voltage-gated L-type Ca channels (LCCs) which raise the local concentration. However, under conditions of Ca overload fluctuations of RyR channels from the closed to the open state can induce spontaneous Ca sparks. In this case an RyR channel opening leads to a local increase in Ca which can diffuse and induce additional openings of the channels in the cluster. This process is highly nonlinear and leads to a substantial increase of local Ca which can, in some cases, diffuse and stimulate nearest-neighbor CRUs. When this occurs a Ca wave can be nucleated which can spread across the cell and induce a substantial release of Ca. It is these release events which are believed to underlie various cardiac arrhythmias.

B. A simple model of stochastic wave nucleation

In this study we will apply a minimal model in order to explore the relationship between the arrangement of CRUs and the nucleation of Ca waves. Given the complexity of the local RyR kinetics in a cluster we will simplify the system by modeling the ith CRU using a state variable η_i, which can be $\eta_i = 0$ (no spark) or $\eta_i = 1$ (spark). To model the stochastic dynamics of Ca sparks we let the state variable obey the reaction scheme

$$0 \underset{\beta_i}{\overset{\alpha_i}{\rightleftharpoons}} 1, \tag{1}$$

where α_i is the rate at which sparks are ignited at site i, and where β_i is the rate at which a spark at that site is extinguished. Since RyR cluster openings are regulated by the local Ca concentration, we will take the forward rate to be $\alpha_i = g_i c_i^\gamma$, where c_i is the local Ca concentration at site i, g_i represents the excitability of that CRU, and γ is an exponent that describes the nonlinear dependence of the spark activation rate on the local Ca concentration. Experimental studies reveal that the open probability of RyR channels is a nonlinear sigmoid function of the local Ca concentration [3,20]. Thus, given the Ca-mediated cooperativity between RyR channels in the cluster, we expect that the rate of spark formation should have a highly nonlinear dependence on the local Ca concentration. To account for this nonlinearity we will set $\gamma = 2$ in this study. Furthermore, we note that in the cell Ca sparks terminate due to inactivation or SR depletion. Here, we focus only on the dynamics of wave nucleation, and neglect the role of slow recovery processes due to a previous excitation.

In this study we will focus on spontaneous Ca waves that occur due to RyR channel openings, and so we will consider the case where the LCC channels are shut. In this case the local Ca concentration at a CRU is given by

$$c_i(t) = c_o + \sum_{j \neq i} h_{ij}(t)\, \eta_j(t), \tag{2}$$

where c_o is the background Ca concentration, and where $h_{ij}(t)$ gives the rise in the local Ca concentration at site i due to an active Ca spark at site j ($\eta_j = 1$). To model interactions between CRUs we note that the solution of the diffusion equation in an isotropic medium requires that the concentration at site i due to Ca released at site j should fall off proportionally to $\exp[-d_{ij}^2/4D(t - t_j)]$. Here, d_{ij} is the distance between the CRUs, D is the effective diffusion coefficient of Ca, and t_j is the activation time at site j. Here, we make the simplification that sites which influence site i are activated at roughly the

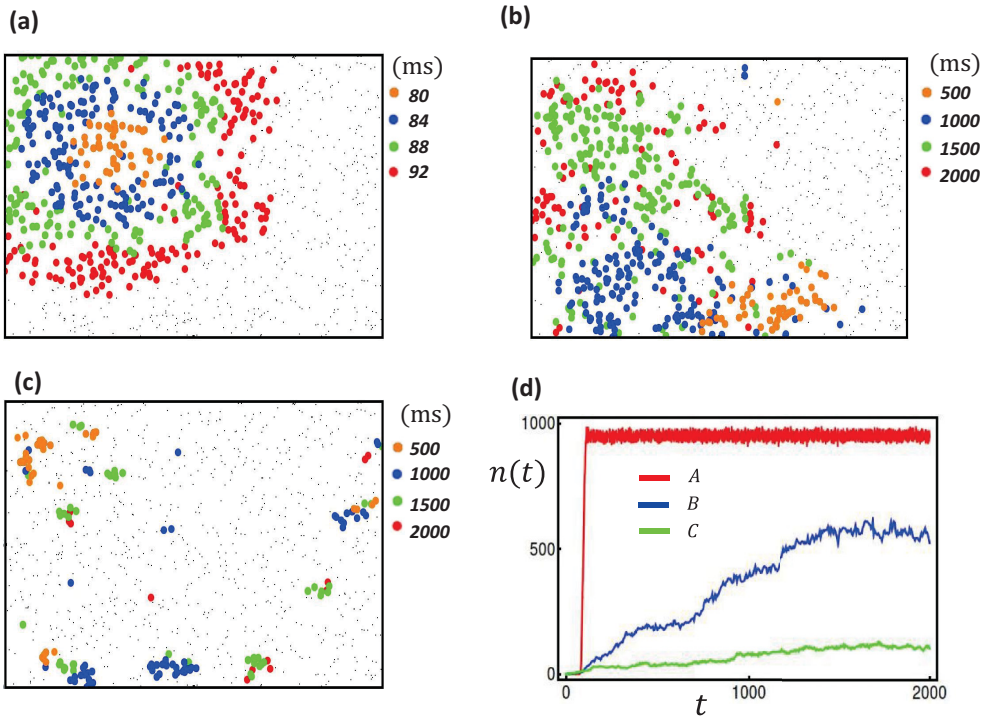

FIG. 2. (Color online) Spatiotemporal evolution of active sites in a system with $N = 1000$ CRUs and $L = 1$. The ith site is placed at location (x_i, y_i), where x_i and y_i are picked from a uniform distribution on the interval $[0,1]$. (a) Ca sparks are nucleated at localized regions and spread rapidly as an advancing front of active sites. In this case system parameters are chosen to be $s = 4$ and $r = 0.3$. Snapshots of active sites at the times shown are indicated. (b) For reduced excitability and coupling ($s = 3$, $r = 0.1$) active sites spread in a diffuse manner and settle in a disordered fluctuating pattern. (c) When the coupling is further reduced only a few sites are activated and randomly distributed in clumps in the system ($s = 1$, $r = 0.8$). (d) The total number of active sites $n(t)$ as a function of time for the three cases shown in (a)–(c). The location of sites is the same for all simulation runs.

same time, so that the weighting of distant sites is mostly determined by the exponential dependence on d_{ij}^2. To model this effect we will consider coupling between CRUs of the form

$$h_{ij} = r_j \exp[-|\vec{x}_i - \vec{x}_j|^2/l^2], \tag{3}$$

where r_j represents the Ca released at site j, $\vec{x}_i$ and $\vec{x}_j$ are the locations of the ith and jth CRUs in the cell, and l is a diffusive length scale. Alternatively, we note that Ca buffers in the intracellular space will also determine the concentration of Ca away from the source. This problem has been addressed in detail [21], and it is found that the concentration away from a source of Ca should decay as $\sim(1/d_{ij})\exp(-d_{ij}/l)$, where l is a length scale that is dependent on the buffer kinetics and diffusivity. In both cases the site-to-site coupling is effectively short ranged and is characterized by a length scale l which will be systematically varied in our model.

C. System parameters

To model the spatial distribution of active sparks in a cell we will study the time evolution of our system in two dimensions (2D). Thus, we consider the dynamics of N CRUs that are placed at random locations on a square of size $L \times L$, so that the ith site is placed at location (x_i, y_i), where x_i and y_i are chosen from a uniform distribution in the interval $[0, L]$. This arrangement introduces a length scale which is the average minimum distance between CRUs. This distance can be estimated to be $d \sim L/2\sqrt{N}$, so that a natural dimensionless parameter that characterizes the system is the ratio $s = l/d = 2\sqrt{N}\, l/L$, which gives a measure of the length scale of diffusive interactions compared to the average CRU spacing. Hereafter, we will refer to the parameter s as the spatial coupling strength. In this study we will consider the case where each CRU is equivalent so that $\alpha_i = \alpha$, $\beta_i = \beta$, $g_i = g$, and $r_i = r$. Also, we take the diffusive length scale to be a constant with $l_{ij} = l$, so that the heterogeneity in the system originates only from the spatial arrangement of CRUs on the plane. The parameter r will be referred to as the excitability of the system since it gives a measure of the amount of Ca released at a CRU. To fix the system parameters we will rely on existing experimental observations of Ca sparks and waves. First, we will assume that Ca can diffuse between nearest neighbors depending on the amount of Ca released at each CRU. At high SR loads we expect that Ca released at a CRU can diffuse to several nearest neighbors so that we will consider spatial coupling in the range $0 < s < 6$. Also, we will also take $c_o = 0.01$ μM and let the spark rate of an isolated CRU be $\alpha \sim 0.001$ ms^{-1}, which is roughly one spark every second. Since $\alpha = g c_o^2$ this will fix $g = 0.5$ ms^{-1} μM^{-2}. Finally, we note that since a Ca spark typically lasts for a duration 20–50 ms, we will take $\beta = 0.05$ ms^{-1}.

D. Spatiotemporal dynamics

In Figs. 2(a)–2(c) we show the spatiotemporal evolution of active sites starting with initial conditions such that all sites are

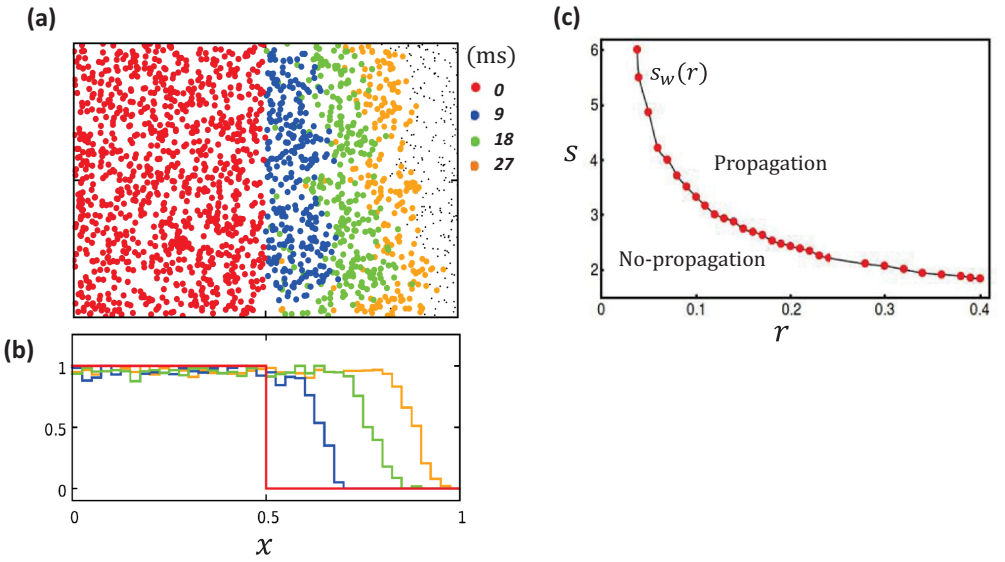

FIG. 3. (Color online) (a) The evolution of a planar front of active sites. Initial conditions are chosen such that $\eta_i = 1$ for $x < 1/2$ and $\eta_i = 0$ for $x > 1/2$. Filled circles represent active sites at the indicated times. System parameters are $s = 4$ and $r = 0.2$. (b) Evolution of wave front is tracked by averaging η_i in the y direction in bins of size $\Delta x = 1/40$. (c) Wave propagation threshold in parameter space.

inactive ($\eta_i = 0$). Our numerical simulations reveal that there are two distinct phases of the system. In one case, illustrated by Fig. 2(a), Ca sparks are nucleated at localized regions of the system and proceed to spread rapidly as an advancing front of active sites, with $\eta_i = 1$, which invades the surrounding inactive region with $\eta_i = 0$. In Fig. 2(a) we show the spatial distribution of active sites for a short time interval following nucleation of the advancing front. In this regime the total number of active sites, denoted as $n(t)$, increases rapidly once a wave is nucleated [Fig. 2(d), red trace], and the system settles to a final steady state where most of the sites are in the active state. In the case where the excitability and coupling are reduced we see that waves are not nucleated in the system [Fig. 2(b)]. Here, the system slowly evolves towards a state where active sites form a sparse random pattern, where each unit fluctuates with time according to the local stochastic dynamics. In this case, the evolution of the spatial pattern does not occur via a coherent activation front but rather in a gradual fashion where the pattern of activity spreads in a diffuse manner. In this case we find that the number of active sites increases on a much slower time scale [Fig. 2(d), blue trace]. As the coupling is reduced further [Fig. 2(c)] the spreading of active sites occurs even more slowly, and settles in a sparse random pattern where only a few sites are active [Fig. 2(d), green trace]. Here, we find that the steady state is governed by clumps of active sites spread randomly throughout the system. These distinct cases are representative of the possible spatiotemporal evolution of the system.

E. The propagation and timing of Ca waves

An important feature of the spatiotemporal dynamics is the nucleation of propagating Ca waves. To analyze the dynamics of waves we study the evolution of a front in 2D that joins a region of high activity with $\eta_i = 1$ with an inactive region with $\eta_i = 0$. Our goal is to determine the conditions for which the planar front advances in our system. To investigate this transition in the most simple setting we chose initial conditions such that all points on our $L \times L$ square with $x \leqslant L/2$ are set to the value $\eta_i = 1$, and all points $x > L/2$ are $\eta_i = 0$ [Fig. 3(a)]. To track the evolution of the front we average η_i in the y direction in bins of size $\Delta x = 1/40$ along the x axis. In Fig. 3(b) we show the time evolution of this projection, showing that fronts can propagate from the active to the inactive state. Analysis of these fronts reveals that for a given excitability r there is a critical coupling s_w, which we will refer to as the front propagation threshold, such that fronts will propagate with $s > s_w$ but remain pinned for $s < s_w$. In Fig. 3(c) we plot the function $s_w(r)$ which separates the propagating and nonpropagating regions of phase space.

To characterize the timing of wave nucleation we chose initial conditions so that all sites are inactive ($\eta_i = 0$), and determine the average waiting time T for a Ca wave to be nucleated in the system. Our criterion for wave nucleation is that the fraction of active sites exceeds 80% of the total number of CRUs in the system. In Fig. 4 we plot the average wave nucleation time, averaged over 100 independent simulations, as a function of the system excitability r, and for a range of values of the spatial coupling s. This result reveals that as the excitability r is reduced the wave nucleation time increases substantially. Specifically, we find that as r approaches the propagation threshold the first passage time T appears to diverge. In practice, simulation times become exceedingly large and we show results only up to a mean waiting time of $T = 1000$ ms.

F. Steady state dynamics

To further characterize the system we have computed the long-time dynamics of active sites. Thus, we compute the time dependence of the average number of active sites, which we define as $\langle \eta(t) \rangle = (1/N) \sum_{i=1}^{N} \eta_i$. Since the steady state

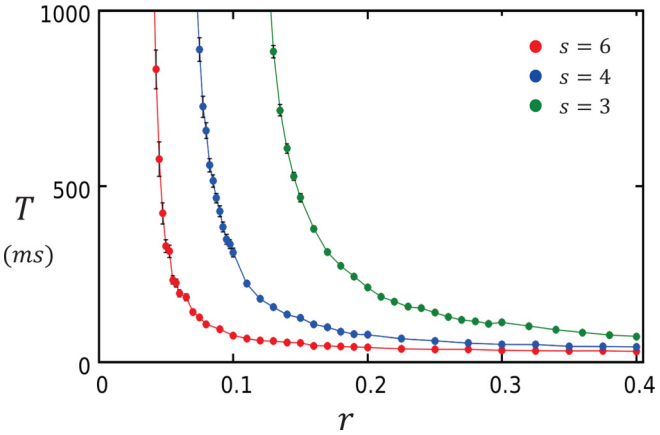

FIG. 4. (Color online) The average wave nucleation time, averaged over 100 independent simulations, as a function of the system excitability r and spatial coupling $s = 3$ (green), $s = 4$ (blue), and $s = 6$ (red).

dynamics depends crucially on initial conditions we will consider the dynamics of $\langle \eta(t) \rangle$ for a broad range of initial conditions. Thus, we consider initial conditions so that the probability that a site is active ($\eta_i = 1$) is taken to be p, and where p will be varied in the range 0 to 1. In Figs. 5(a)–5(c) we show the time evolution of $\langle \eta \rangle$ for a range of excitability r, and where the coupling is fixed at $s = 4$. Based on these simulations we identify three distinct steady state behaviors. For small values of r we find that the system evolves towards a low-activity state where $\langle \eta \rangle \sim 0$ [Fig. 5(a)], independently of initial conditions. As r is increased further we find that $\langle \eta \rangle$ evolves towards multiple values depending upon the initial conditions [Fig. 5(b)]. Hereafter, we will refer to this regime as the multistable phase. In Fig. 5(e) we show snapshots of the active sites at steady state. In this regime, different initial conditions evolve towards distinct nonhomogeneous steady states. Finally, for larger r values the system again evolves to a state where $\eta \sim 1$ independently of initial conditions [Fig. 5(c)]. To further quantify this behavior, in Fig. 5(d) we plot the value of $\langle \eta \rangle$ after a time of $t = 5000$ ms, for a range of initial conditions. We have taken the value at this time since it is much longer than the transient dynamics observed, and the system appears to have reached steady state. Indeed, we find that for a range of excitabilities ($r_a < r < r_b$) $\langle \eta \rangle$ can attain several distinct values, while outside this range $\langle \eta \rangle \sim 0$ for $r < r_a$ and $\langle \eta \rangle \sim 1$ for $r > r_b$. To quantify this finding we have also computed the variance σ of the steady state value of $\langle \eta \rangle$. Hence, we compute $\sigma = \sqrt{\overline{\langle \eta \rangle^2} - \overline{\langle \eta \rangle}^2}$, where $\bar{x}$ denotes the sample average of x over the different initial conditions. As shown in Fig. 5(d) (red line) the variance σ increases substantially in the multistable phase of the system ($r_a < r < r_b$).

Our simulations indicate that above the wave propagation threshold the system evolves towards the active state where

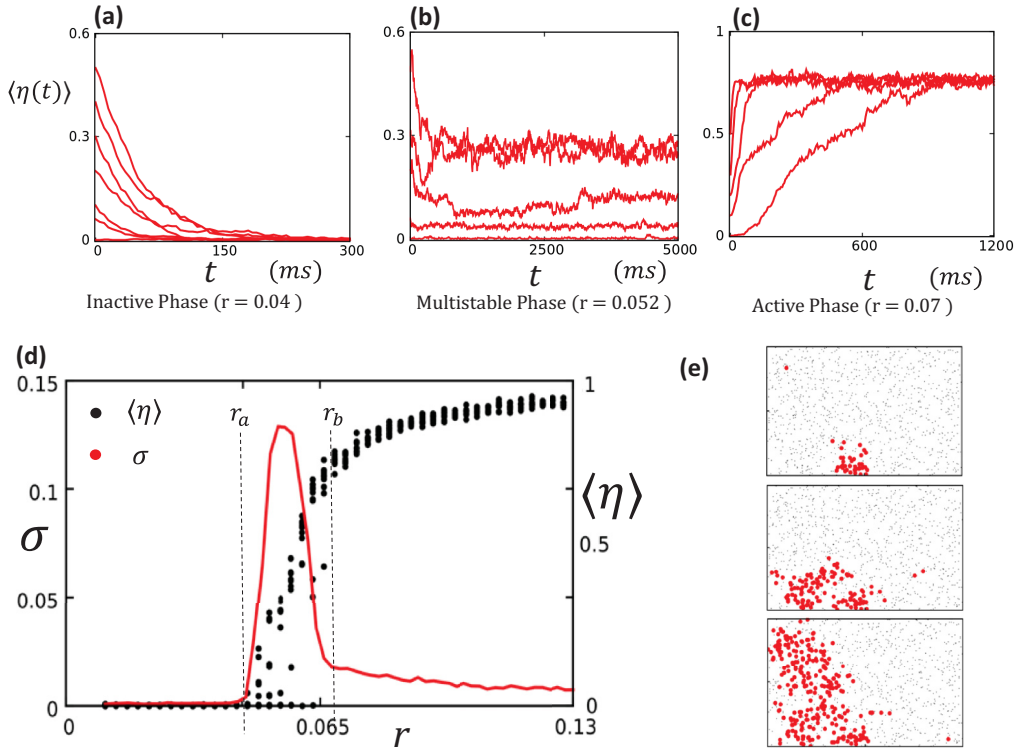

FIG. 5. (Color online) The average activity $\langle \eta(t) \rangle$ vs time for a range of initial conditions. Initial conditions are chosen so that (0,2,4,6,8,10,20,30,40,50)% of the sites are active at time $t = 0$. (a) Inactive phase with $r = 0.04$. (b) Multistable phase with $r = 0.052$. (c) Active phase with $r = 0.07$. In all cases coupling is set to $s = 4$. (d) Plot of $\langle \eta \rangle$ at time $t = 5000$ ms (black circles) as a function of r. For each parameter value the system is simulated for the ten initial conditions. Using the same data the variance σ is computed (red line). (e) Snapshots of three distinct steady state patterns for the multistable case shown in (b). Red circles correspond to active sites.

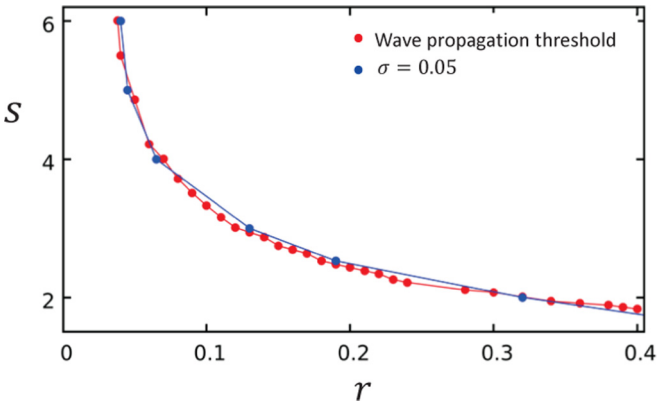

FIG. 6. (Color online) The wave propagation threshold (red line) and the transition line separating the monostable active and the multistable phases. The onset of the multistable phase is determined by finding the parameter r where the variance σ just exceeds 0.05.

$\langle\eta\rangle \sim 1$. Thus, we expect that the transition from the active to multistable phase, at $r = r_b$, should coincide with the wave propagation threshold. To check this hypothesis we have compared the wave propagation threshold to the onset of the multistable phase. To determine the onset of the multistable phase we note that the variance σ rises as r is decreased to $r = r_b$ [Fig. 5(d)]. Thus, an accurate marker for the onset of multistability is the value of r such that the variance has risen to the value $\sigma = 0.05$. In this way we can compute a quantitative estimate for the onset of the multistable phase. In Fig. 6 we have plotted the onset of the multistable phase along with the wave propagation threshold. Indeed, we find that these two lines are very close to each other. This result indicates that, as expected intuitively, the onset of the multistable phase coincides with the threshold for wave propagation.

III. MEAN-FIELD THEORY

A. Deterministic mean-field theory

The numerical simulations of our stochastic spark model reveal rich spatiotemporal properties. In order to understand basic features of the system we develop a simplified mean-field theory which will shed light on various aspects of the dynamics. Let us first define the spark probability $P_i(t)$ to be the probability that the ith CRU is active $[\eta_i(t) = 1]$ at time t. The stochastic dynamics is then governed by the master equation

$$P_i(t+\tau) = [1 - P_i(t)](\alpha_i\tau) + P_i(t)(1 - \beta_i\tau), \qquad (4)$$

where $\alpha_i\tau$ and $\beta_i\tau$ are the transition probabilities that site i makes a $0 \to 1$ or $1 \to 0$ transition in the time interval τ. To simplify the dynamics we will make the approximation that the state variables can be replaced by their averages so that $\eta_j \approx P_j$, and the local Ca concentration can be approximated by $c_i \approx c_o + \sum_{j\neq i} h_{ij} P_j(t)$. In the continuum limit the master equation then simplifies to the system of equations

$$\frac{dP_i}{dt} = g_i\left(c_o + \sum_{j\neq i} h_{ij}P_j\right)^2 (1 - P_i) - \beta_i P_i, \qquad (5)$$

which describes the time evolution of the spark probability $P_i(t)$.

B. Steady state dynamics of the mean-field equations

To analyze the dynamics of the mean-field equations we first consider steady state solutions to the N nonlinear equations given in Eq. (5). To distinguish steady state solutions we keep track of the average site probability defined here as $\langle P(t)\rangle = (1/N)\ \sum_{i=1}^{N} P_i(t)$, and denote the steady state occupation probability as $\langle P\rangle_\infty = \langle P(t \to \infty)\rangle$. To capture the system behavior over a wide range of parameters we will compute $\langle P\rangle_\infty$ vs the excitability r, for different values of the dimensionless ratio s. As in the full stochastic model Eq. (5) can have multiple steady state solutions, which can be reached depending upon the initial conditions chosen. Thus, we consider a range of initial conditions of the form $P_i = p + \xi_i$, where p is an average that will be varied, and where ξ_i is a uniformly distributed random number with an average $\langle\xi\rangle \ll p$. By considering the time evolution of an ensemble of initial conditions, with varying p and $\langle\xi\rangle$, we can then explore the possible steady state solutions to Eq. (5). Our main results are summarized in Fig. 7(A) where we have plotted $\langle P\rangle_\infty$ vs r for a fixed coupling of $s = 2.5$. We find that for $r < r_a$ then there is effectively only one steady state solution vector P_i with $\langle P\rangle_\infty \sim 0$ [Fig. 7(a)]. This solution corresponds to the inactive state of the system where the steady state probability of active sites is low. For larger excitability r we find that there is a region of parameter space between r_a and r_b where there are multiple steady state solutions which can be reached depending upon the initial conditions [Fig. 7(b)]. However, for larger excitability $(r_b < r < r_c)$ we find that these multiple states collapse into effectively two distinct solutions. In this regime the system is bistable and can be in either the active state $(\langle P\rangle_\infty \sim 1)$ where most sites are active, or the inactive state where the system is quiescent $(\langle P\rangle_\infty \sim 0)$ [Fig. 7(c)]. For even larger excitability $r > r_c$ the lower branch vanishes and the system evolves to a single unique solution in which $\langle P\rangle_\infty \sim 1$ [Fig. 7(d)]. In order to characterize the steady state behavior of the mean-field equations we have constructed the full phase diagram of the mean-field theory. In Fig. 8 we plot the boundaries separating the monostable, bistable, and multistable phases of the mean-field equations.

As in the full stochastic model we find that the mean-field equations also possess propagating front solutions. To investigate the wave propagation threshold we simulate the time evolution of a planar front in 2D which joins the active $(P_i = 1)$ and quiescent $(P_i = 0)$ states. In Fig. 8 we show the wave propagation threshold in parameter space (red dashed line). Above this line a planar front of active sites invades the region of inactive sites, while below, the front remains pinned or is extinguished. Indeed, we find that, as in the full stochastic model, the wave propagation threshold coincides with the bistability-multistability transition line.

C. The role of fluctuations

A basic limitation of the mean-field theory is that it neglects fluctuations. Thus, key features of the full stochastic

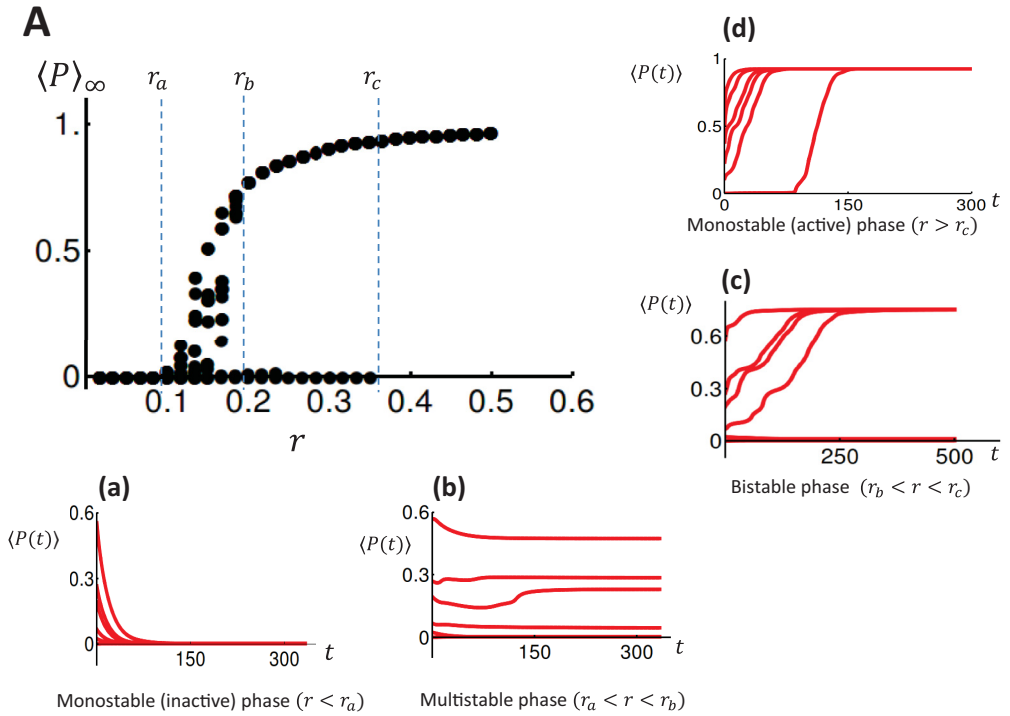

FIG. 7. (Color online) Dynamics of the mean-field theory. (A) Steady state average site probability $\langle P\rangle_\infty$ vs r computed for randomly chosen initial conditions. In this simulation the coupling parameter is fixed at $s = 2.5$ and steady state is taken to be the solution at time $t = 1000$ ms. The number of sites is taken to be $N = 500$ and the ODEs are integrated with a time step of $dt = 0.1$ ms. (a)–(d) Sample traces of $\langle P(t)\rangle$ vs time t showing evolution to (a) monostable inactive, (b) multistable, (c) bistable, and (d) monostable active phase.

model, such as wave nucleation due to fluctuations, cannot be described in this picture. To investigate the role of fluctuations we will introduce a noise term to Eq. (5). Thus, we will consider equations of the form

$$\frac{dP_i}{dt} = g_i\left(c_o + \sum_{j\neq i} s_{ij}P_j\right)^2(1-P_i) - \beta_i P_i + \xi_i(t), \quad (6)$$

where $\xi_i(t)$ is a Gaussian noise term that satisfies $\langle \xi_i(t)\xi_j(t')\rangle = D^2\delta_{ij}\delta(t-t')$, and where $\langle \xi_i(t)\rangle = 0$. In this scenario the deterministic equations are driven by uncorrelated noise which should mimic the effect of stochastic fluctuations from the reaction scheme given by Eq. (1). In this study we seek to explore the qualitative behavior of Eq. (6) and so we will consider the system behavior for a wide range of noise strengths. Thus we will choose our noise amplitude so that $D = \sqrt{\langle \xi^2\rangle}$ is in the range 10^{-4}–10^{-2}. Equation (6) is solved directly using a standard Euler scheme [22], where it is necessary to introduce a boundary condition that fluctuations cannot induce unphysical probabilities below zero. Thus, during the numerical time stepping we impose the condition that $P_i = 0$ when $P_i < 0$.

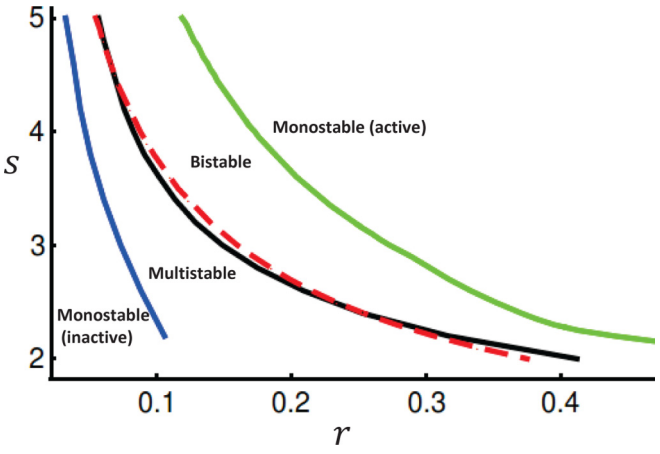

FIG. 8. (Color online) Phase diagram of the mean-field equations showing the phase boundaries between the indicated states. The red dashed line corresponds to the wave propagation threshold. Wave propagation threshold is computed by choosing initial conditions such that $P_i = 0$ for sites with location $x_i < 1/2$, and $P_i = 1$ for $x_i > 1/2$. We then sum the average probability on a strip with $0.9 < x_i < 1$ denoted as P_w. If $P_w > 0.5$ within a simulation time of $t = 1000$ ms then the planar front is said to have propagated to the end of the system.

To explore the behavior of Eq. (6) we will compute the long-time dynamics of the average probability $\langle P(t)\rangle$. First, we note that the deterministic ordinary differential equations (ODEs) [Eq. (5)] reach steady state in a time $t \sim 100$ ms. Thus, we will approximate the steady state average probability to be $\langle P\rangle_\infty = \langle P(t = 1000 \text{ ms})\rangle$. In Fig. 9(a) we show $\langle P\rangle_\infty$ vs r for a range of values of the noise amplitude D. We find that as D is increased, the range of excitability r, where bistability and multistability are observed, is substantially reduced. In

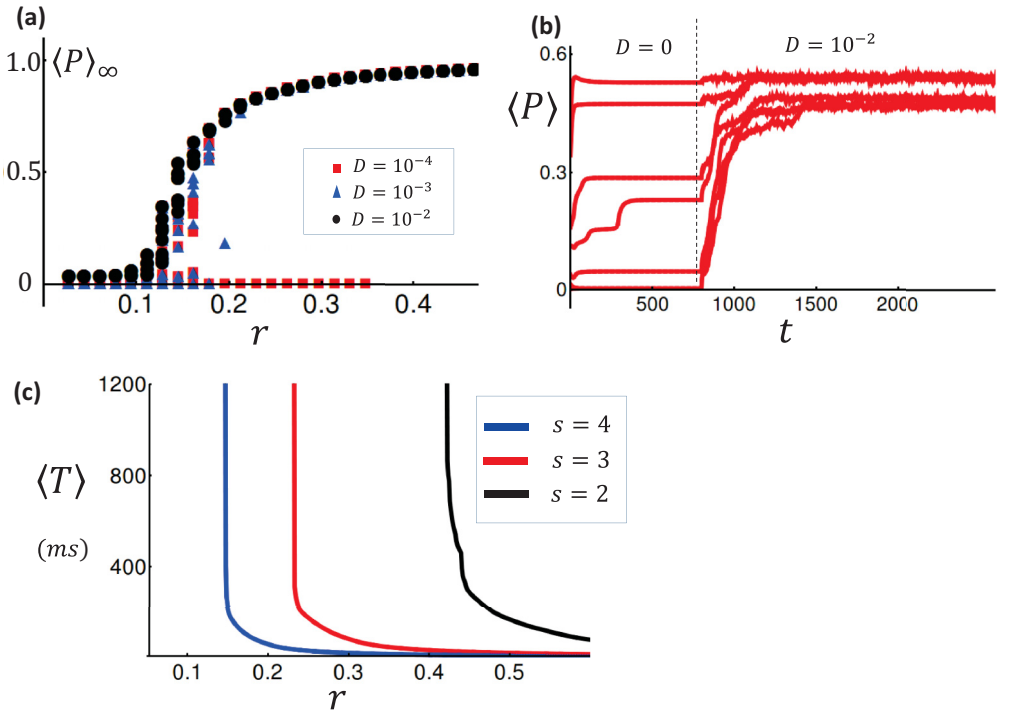

FIG. 9. (Color online) Properties of the mean-field equations with noise. (a) Average site probability $\langle P\rangle_\infty$ vs r computed for ten randomly chosen initial conditions. Here, $\langle P\rangle_\infty$ is taken to be the average site probability evaluated at time $t = 1000$ ms. Noise strength is shown on the inset and spatial coupling is set to $s = 2.5$. ODEs are integrated using a time step of $dt = 0.1$. (b) Time dependence of $\langle P(t)\rangle$. At $t = 800$ ms noise strength is increased from $D = 0$ to $D = 10^{-2}$. Excitability is fixed at $r = 0.16$. (c) Mean first passage time to wave nucleation computed with the stochastic mean-field equations. Noise strength is fixed at $D = 10^{-2}$.

particular, for $D = 10^{-2}$ the bistable regime is eliminated and the dispersion of the multistable phase is reduced. The reason for this decrease in dispersion is illustrated in Fig. 9(b) where we show the effect of noise on the temporal evolution of the system. In this simulation we have chosen $r = 0.16$ so that the deterministic system is in the multistable phase. For times $t <$ 800 ms we set $D = 0$ and let the system evolve towards distinct steady state values depending upon the initial conditions. For times $t > 800$ ms we turn on noise so that $D = 10^{-2}$ and observe that $\langle P(t)\rangle$ evolves towards a smaller set of steady state values. Here, we find that the steady state behavior attained in the deterministic limit is unstable to noise perturbations so that a new set of steady state values is attained once the noise is turned on. In Fig. 9(c) we plot the mean waiting time to wave nucleation when the noise amplitude is $D = 10^{-2}$. Indeed, consistent with our stochastic model (Fig. 4), we find that the mean waiting time diverges rapidly as the excitability is reduced towards the wave propagation threshold. These numerical results indicate that the mean-field equations with noise capture key features of our stochastic system.

D. Linear stability analysis

Our numerical analysis of the deterministic mean field equations [Eq. (5)] reveals a complex phase diagram. A distinct feature of the system is that for large excitability $r > r_c$ the steady state solution with $P_i \approx 0$ becomes unstable, and the system always evolves towards the fully active state with $P_i \approx 1$. To analyze this transition we consider the stability of the $P_i \approx 0$ solution. In this case we expand Eq. (5) near the steady state solution p_i^* so that $P_i = p_i^* + u_i$, where u_i is a small perturbation. Expanding to linear order in u_i gives the linear system of equations

$$\frac{du_i}{dt} = -[\beta_i + g_i\,(c_o + q_i)^2]u_i + 2g_i(1 - p_i^*)(c_o + q_i)v_i, \tag{7}$$

where $q_i = \sum_j h_{ij} p_j^*$, and where $v_i = \sum_j h_{ij} u_j$. Thus, the stability of the low-activity state is dictated by the system of equations $\dot{u}_i = \sum_j Q_{ij} u_j$ where

$$Q_{ij} = -[\beta_i + g_i(c_o + q_i)^2]\delta_{ij} + 2g_i(1 - p_i^*)(c_o + q_i)h_{ij}. \tag{8}$$

The time evolution of the system is then given by the linear combination

$$\vec{u}(t) = \sum_k a_k e^{\lambda_k t}\,\vec{\phi}_k, \tag{9}$$

where λ_k and ϕ_k are the eigenvalues and eigenvectors of the matrix Q_{ij}. Thus, the quiescent state is unstable when the maximum eigenvalue, which we denote here as λ_1, satisfies the condition $\lambda_1 \geqslant 0$.

To simplify the analysis further we note that the steady state occupation probabilities are small so that $p_i^* \sim 0$ and $1 - p_i^* \sim 1$. We will also assume that each site is identical so that $r_i = r$ and $g_i = g$. Finally, we will make the assumption that the terms $q_i = \sum_j h_{ij} p_j^*$ do not vary substantially from site to site. We have checked this assumption numerically and find that site-to-site variations in q_i have little effect on

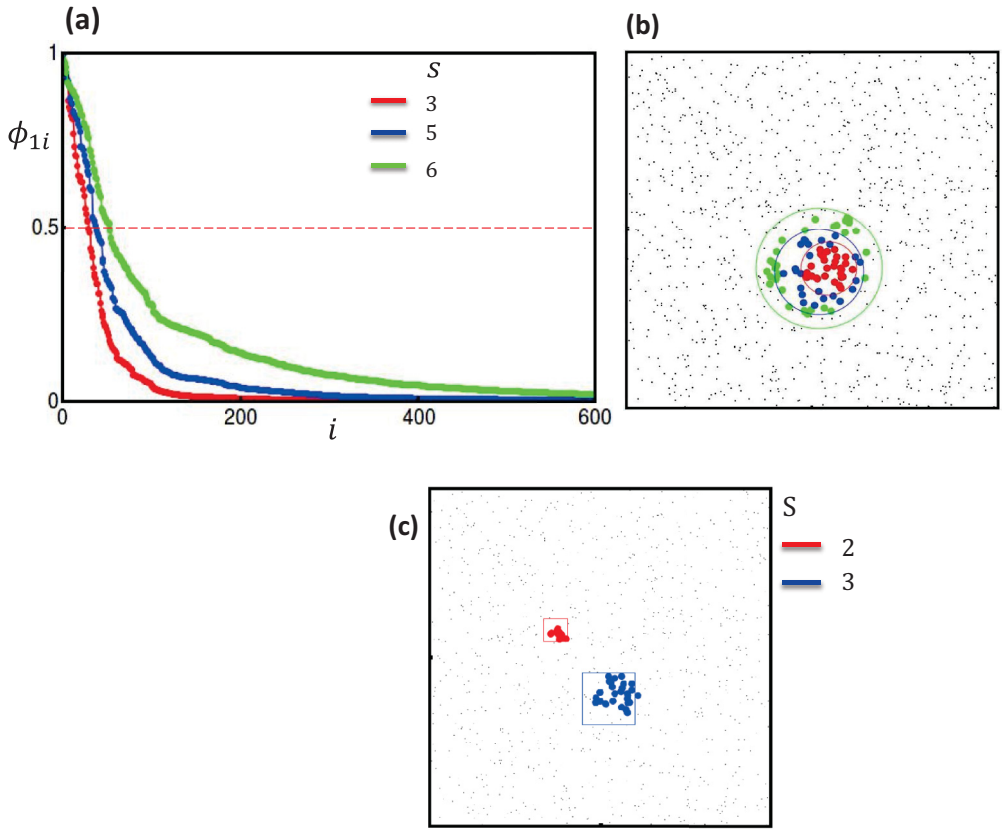

FIG. 10. (Color online) (a) Ordered components of the leading eigenvector $\vec{\phi}_1$, with elements normalized so that the maximum is 1. The system size is taken to be $N = 1000$. (b) Eigenvector components with magnitude larger than 0.5 plotted in the space of points for $s = 3$ (red), $s = 5$(blue), and $s = 6$ (green). (c) Correspondence between high-density regions and eigenvector localization. Blue (red) circles correspond to leading eigenvector components with magnitude larger than 0.5 for parameters $s = 2(s = 3)$. Squares are the regions of highest release site density.

the leading eigenvalues and eigenvectors of the matrix Q_{ij}. Hence, we will make the replacement $q_i \to \langle q \rangle$, where $\langle q \rangle = (1/N)\sum_i q_i$ is the site average. This gives an approximation

$$Q_{ij} \approx -[\beta + g(c_o + \langle q \rangle)^2]\delta_{ij} + 2gr(c_o + \langle q \rangle)\, C_{ij}, \quad (10)$$

where $C_{ij} = \exp[-|\vec{x}_i - \vec{x}_j|^2/l^2]$ is the connectivity matrix. The leading eigenvalue is given by $\lambda_1 = -[\beta + g(c_o + \langle q \rangle)^2] + 2gr(c_o + \langle q \rangle)\lambda_c$, where λ_c is the leading eigenvalue of the matrix C_{ij}, and where the spatial evolution of the system is governed by the eigenvector which corresponds to λ_c.

E. Localization of eigenvectors

The linear stability analysis allows us to understand the spreading of activity from an initially low active state. According to Eq. (9) the initial spreading dynamics will be dictated by the eigenvectors which correspond to the largest eigenvalues of the connectivity matrix C_{ij}. Here, we will explore the spatial structure of these eigenvectors in order to determine the nucleation sites of Ca waves. To determine the shape of the leading eigenvector $\vec{\phi}_1$ we rescale the eigenvector components, denoted as ϕ_{1i}, so that the component with the maximum magnitude has the value 1. We then plot ϕ_{1i} vs i where the ith component is that component with the ith largest magnitude. The ordered magnitudes for a system of $N = 1000$ sites, and for different values of the coupling parameter s, are shown in Fig. 10(a). This result indicates that eigenvector components are strongly peaked at a small fraction of sites in the system. In this case we find that the eigenvector amplitudes are concentrated on fewer than 5% of the sites in the system. In order to visualize the spatial distribution of the leading eigenvector we have also plotted all spatial sites with eigenvector components with magnitude $\phi_{1i} > 0.5$. In Fig. 10(b) we show the spatial distribution of these sites for different values of the coupling parameter s. This result demonstrates that the eigenvectors of the connectivity matrix C_{ij} are localized at specific regions in the system.

To explore further the factors that determine the sites of eigenvector localization we have computed the spatial distribution of the density of release sites. First, we note that to compute the density it is necessary to chose an appropriate length scale. A natural length scale to pick is the effective localization length of the leading eigenvector, which we will denote here as l_c. Thus, we measure the effective radius of the the leading eigenvector by computing the radius of the smallest circle that encloses all sites with $\phi_{1i} > 0.5$. Using this length scale l_c we then compute the density within squares of size $l_c \times l_c$. In Fig. 10(c) we plot the leading eigenvector for a particular configuration of sites, and where we have picked the dimensionless parameter to be $s = 2$ and $s = 3$. Here, we observe that the region of

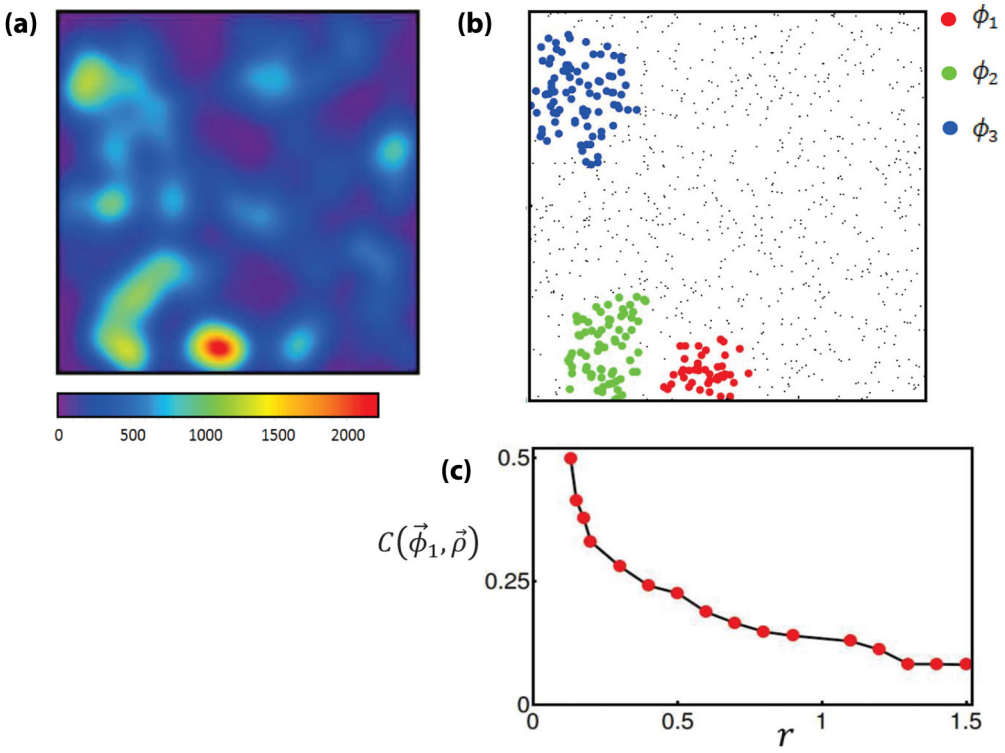

FIG. 11. (Color online) Density of nucleation sites and eigenvectors. (a) Spatial density of wave nucleation sites computed using 20 000 simulation runs. Color bar indicates the number of waves nucleated. (b) Sites with magnitude $\phi_i > 0.1$ for the eigenvectors corresponding to the three highest eigenvalues. (c) Pearson correlation coefficient between nucleation density vector $\vec{\rho}$ and the largest eigenvector $\vec{\phi}_1$ plotted as a function of the excitability parameter r.

localization of the leading eigenvector is different in the two cases, even though the underlying spatial distribution of points is identical. On the same plot we identify the highest density of points within squares of size $l_c \times l_c$. Indeed, we find that the leading eigenvector coincides with the region of highest density at the given scale. This result demonstrates that the leading eigenvectors of the connectivity matrix are localized at high-density regions.

IV. THE SITES OF Ca WAVE NUCLEATION

Our linear stability analysis reveals that the inactive state ($\eta_i = 0$) is unstable when $\lambda_1 > 0$, and that spreading will be localized on a few sites determined by the leading eigenvector $\vec{\phi}_1$. In this section we will proceed directly to the full stochastic model to determine the spatial distribution of nucleation sites. To determine these nucleation sites we simulate the stochastic evolution of the initially quiescent state and determine the spatial distribution of active sites at the onset of wave nucleation. To achieve this, our approach was to first determine the time t_a where the number of active sites reached 3% of the steady state number of active sites (n_∞) after wave nucleation. This simulation is repeated for M times, and for each site i in our system we compute the ratio $\rho_i = n_i(t_a)/M$, where $n_i(t_a)$ is the total number of instances when site i is active at the nucleation time t_a. Using this approach we can construct the spatial density of active sites at the onset of wave nucleation. In Fig. 11(a) we show the spatial density of active sites in our system computed using $M = 20\,000$ simulation runs. In this simulation we find that most of the waves are nucleated at a specific localized region in the system (see density scale). In Fig. 11(b) we plot all sites with magnitude greater than 0.1 for the eigenvectors corresponding to the three largest eigenvalues.

Our numerical simulations reveal strong correlations between the leading eigenvectors of the connectivity matrix C_{ij} and the density of Ca wave nucleation sites. To check this prediction quantitatively we have computed the Pearson correlation coefficient between the leading eigenvector $\vec{\phi}_1$ and the density vector $\vec{\rho}$ at the onset of wave nucleation. To compare these two vectors we compute their similarity using the standard Pearson correlation coefficient which is given by the quantity

$$\mathrm{C}(\vec{\rho},\vec{\phi}_1) = \frac{\sum_i^N (\rho_i - \langle\rho\rangle)(\phi_{1i} - \langle\phi\rangle)}{\sqrt{\sum_i^N (\rho_i - \langle\rho\rangle)^2}\sqrt{\sum_i^N (\phi_{1i} - \langle\phi\rangle)^2}}, \qquad (11)$$

so that $C(\vec{\rho},\vec{\phi}_1) \sim 1$ or 0 if the vectors are strongly correlated or uncorrelated. In Fig. 11(c) we plot the Pearson correlation coefficient C vs the excitability r, showing that the correlation increases as the excitability is decreased towards the wave propagation threshold. This result demonstrates that the leading eigenvector of the connectivity matrix becomes increasingly predictive of the spatial distribution of wave nucleation sites as the system excitability is decreased.

The relationship between the leading eigenvector and the nucleation site probability distribution should also hold in

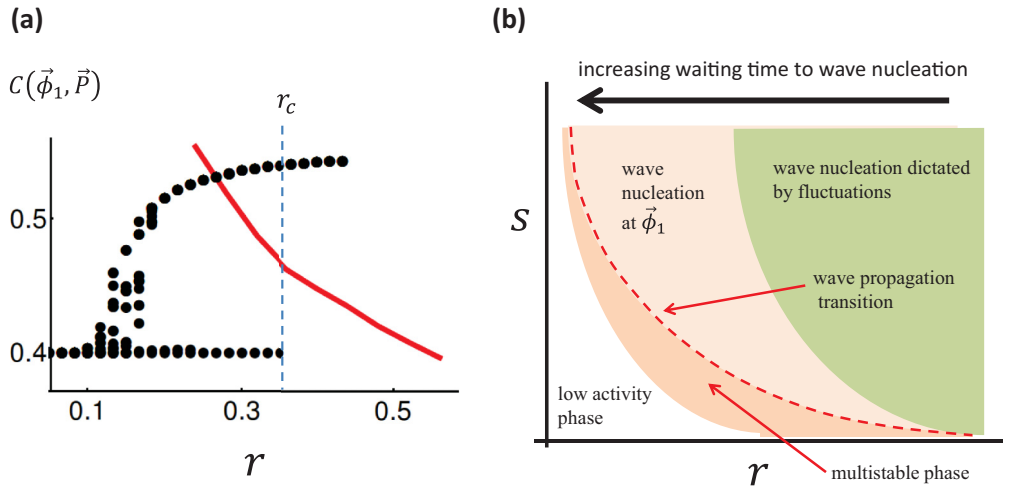

FIG. 12. (Color online) (a) The Pearson correlation between the leading eigenvector $\vec{\phi}_1$ and the site probability $\vec{P}(t_a)$ taken at a time t_a where $\langle \vec{P}(t_a) \rangle = 0.1$ (red line). The initial conditions are chosen so that 10% of sites are assigned the value $P_i(t=0) = \xi_i$, where ξ_i is taken from a uniform distribution in the range [0,0.5]. Averaging is taken over 5000 simulation runs. For reference we have overlayed the steady state $\langle P \rangle_\infty$ of the deterministic mean-field theory (black circles). Dashed line indicates the excitability $r = r_c$ separating the monostable and bistable regimes. (b) Illustration of the system phase diagram.

the mean-field theory with noise [Eq. (6)]. To check this result we chose parameters above the wave propagation threshold, and consider the time evolution of a sparse initial pattern with $\langle P \rangle \sim 0$. In this parameter regime we measure the time t_a when the average site probability has increased to $\langle P(t_a) \rangle = 0.1$. We then compute the Pearson correlation $C(\vec{P}(t_a), \vec{\phi}_1)$ where $\vec{P}(t_a)$ is the probability of release sites at the onset of wave nucleation. In Fig. 12(a) we plot C vs r, which shows that the correlation increases as the excitability r is decreased. On the same graph we overlay the steady state average $\langle P \rangle_\infty$ computed using the deterministic mean-field theory. Here, we note that the leading eigenvector is predictive of the wave initiation sites for $r < r_c$, which is the regime in which the leading eigenvector is stable ($\lambda_1 < 0$). These results indicate that the leading eigenvector is predictive of the sites of nucleation up to the wave propagation threshold.

V. DISCUSSION

In this paper we have developed a simplified stochastic model of Ca wave nucleation in a cardiac cell. In this setting, the spatiotemporal dynamics can be characterized using the excitability r, which is the amount of Ca released during a spark, and the spatial coupling s, which is the ratio of the distance Ca ions diffuse during a spark to the average spacing between release sites. In terms of these parameters we show, in Fig. 12(b), an illustration of the phase diagram of the system. Here, we identify a critical line (red dashed line) that separates pinned and propagating excitation fronts. This transition line has been observed in previous studies and is due to the spatial discreteness of the system [12,13]. In effect, the spatial separation between release sites ensures that there is always a critical excitability below which waves cannot propagate. A numerical study of the regime of propagation revealed that the waiting time to a nucleation event diverges as the excitability is reduced towards the propagation threshold. Furthermore, we show that as the critical line is approached wave nucleation tends to occur at regions in which the leading eigenvector of the connectivity matrix C_{ij} is peaked. In this regime it is the spatial arrangement of release sites that dictates where fluctuations initiate wave nucleation. However, further away from the critical line there is a regime of high excitability where small fluctuations are sufficient to nucleate waves. In this regime fluctuations dominate nucleation kinetics and the arrangement of CRUs does not play an important role. In particular, in the limit of large r wave nucleation occurs at the first $0 \to 1$ transition, so that wave nucleation occurs at any site with equal probability. Now, below the critical line we also observe rich dynamical behavior. In particular, we identify a multistable phase where the steady state activity levels form random patterns that are dictated by initial conditions. In this regime waves do not propagate and so there is no mechanism to drive the system to the fully active state. On reducing the excitability further we also identify a phase where the system is trapped in a low-activity state. In this regime cooperativity between release sites is weak and the system can be described as a collection of independent sites.

The rich spatiotemporal dynamics of our system can be explained by the interplay between noise and the time evolution of the deterministic mean-field equations [Eq. (5)]. For large excitability ($r > r_c$) the deterministic mean-field equations possess propagating wave solutions, and the quiescent state is unstable since $\lambda_1 > 0$. In this regime wave nucleation is deterministic and the presence of advancing fronts ensures that the same steady state is reached independently of initial conditions. In effect, propagating fronts smooth out inhomogeneities and the presence of noise does not change the qualitative behavior of the system dynamics. Now, for $r_b < r < r_c$ the deterministic mean-field equations exhibit bistability since the quiescent state with $P_i \sim 0$ is stable ($\lambda_1 < 0$). In this regime fronts advance in the system so that the active branch with $\langle P \rangle \sim 1$ can be reached only if there is a sufficiently large region of active sites. Now, in the presence of noise,

fluctuations can induce a large enough region of active sites that will propagate in the system. Thus, the time evolution of the quiescent state will be governed by stochastic wave nucleation, which is characterized by a mean-first-passage time T. In effect, bistability will be observed in the fully stochastic system only if the state of the system is evaluated at a time $t < T$. For $t > T$ wave nucleation will likely occur and bistability will not be observed, as the system will evolve towards the active branch. Now, in the regime $r_a < r < r_b$ the deterministic mean-field equations evolve towards a multitude of possible steady states. In this phase we find that active fronts are pinned, so that different steady states can be reached depending on the initial configuration of active sites. Now, in the presence of noise we find that the system evolves towards a smaller set of steady states [Fig. 9(b)]. This is because noise fluctuations can destabilize a subset of the steady states that are reached by the deterministic evolution. A pertinent analogy to this behavior is found in the theory of spin glasses where a disordered system possesses a rugged energy landscape with a large number of energy minima [23]. There, fluctuations due to temperature can induce transitions between local minima, and the long-time behavior of the system is governed by the slow dynamics of stochastic escape between these local minima. However, this dynamics is exceedingly slow since the mean time to escape can be exponentially long. In this case the system is said to exhibit "glassy" behavior since the system ages over a long time scale, and steady state may not be reached in a tractable simulation time. In effect, the presence of noise should drive the system to a unique steady state, but this will likely take an exceedingly long time. Finally, for $r < r_a$ a wide range of initial conditions evolve to the same quiescent state with $P_i \sim 0$. In this regime there is effectively only one distinct steady state and noise does not change the system behavior.

Our mean-field analysis provides a precise picture of the sites of wave nucleation. In the case when $\lambda_1 > 0$ wave nucleation is deterministic and the sites of nucleation tend to occur at the regions where $\vec{\phi}_1$ is localized. However, in the case where the quiescent state is stable ($\lambda_1 < 0$) we find that the leading eigenvector is still predictive of the sites of nucleation. In fact, our numerical analysis showed that as r is decreased towards the propagation threshold, the correlation between the leading eigenvector and the sites of wave nucleation increases. This result can be explained from the fact that small fluctuations around the quiescent state evolve according to Eq. (10). Thus, fluctuations which occur at regions where $\vec{\phi}_1$ is localized will decay exponentially at the rate λ_1, which is the slowest decay rate in the system. In effect, the leading eigenvectors identify preferred regions in the cell where noise fluctuations are most likely to initiate a propagating Ca wave. These results reveal that the eigenvalues and eigenvectors of the connectivity matrix play a crucial role in the nucleation dynamics of the system.

Experimental studies have shown that Ca waves can nucleate at specific sites in the cell. In particular, Marchant and Parker [17] imaged Ca waves in the *Xenopus* oocyte and analyzed the source of wave nucleation. Indeed, they found that Ca waves were nucleated at regions of higher release site density. Also, these sites had a higher than average frequency of spontaneous firing indicating a higher excitability. Thus, these experiments reveal that both density and excitability play a crucial role in determining those regions in the cell which are more likely to initiate a Ca wave. Our model analysis predicts that these sites of wave nucleation correspond to the region at which the leading eigenvector is localized. Indeed, we find numerically that the leading eigenvector $\vec{\phi}_1$ tends to localize in regions of higher density. Furthermore, we have explored the role of a heterogeneous distribution of excitabilities (g_i), and find that indeed $\vec{\phi}_1$ will tend to localize in regions of high excitability. However, we have not explored in detail the competition between density and excitability in determining the sites of localization. Interestingly, Marchant and Parker also found that the ability of specific sites to nucleate waves was more prominent when the interval between Ca waves was longer. This result is consistent with our main finding that the leading eigenvector becomes more predictive of the nucleation sites as the system excitability is reduced. Hence, these experiments confirm our finding that the spatial arrangement of release sites becomes more prominent at reduced excitability.

An important limitation of this study is that we have modeled a Ca spark as a simple stochastic on-off process. However, in a cardiac cell, excitation of a Ca spark depends on recovery from inactivation of the RyR channel, or the replenishing of the SR load following Ca release. These dynamical processes introduce refractoriness to each site and will therefore play a crucial role in the location and timing of Ca waves. For example, experiments from Nivala *et al.* [15] have shown that at high external Ca, Ca waves are nucleated periodically at specific sites in the cell. However, when the external Ca is decreased then waves tended to nucleate at random sites in the cell. This result is in contrast to the findings of Marchant and Parker who found that as the excitability is reduced then waves tended to originate at specific sites in the cell. This difference is likely due to the fact that the Ca waves observed in oocytes have a period larger than 10 s, which is likely much larger than the refractory period of release sites. Thus, in this case the initiation of Ca waves is independent of the recovery kinetics, and nucleation sites are dictated by the excitability and arrangement of release sites. On the other hand, Nivala *et al.* observed repetitive waves with a period $\sim$1 s. In this case, it is likely that recovery kinetics played a crucial role in determining the sites of wave nucleation. In fact, it is likely that the sites of wave initiation occurred at those regions in which the recovery kinetics was fastest. In the case that recovery kinetics is dictated by the refilling of the SR network, then these sites likely correspond to regions of the cell with a higher density of SR calcium transport ATPase (SERCA) channels, which are responsible for pumping Ca back into the SR. In this study we have not considered the role of refractoriness, and therefore our analysis applies only in the case when the refractory time is much less than the average waiting time for a wave nucleation event. This is likely the reason why our theoretical results are in excellent agreement with the findings of Marchant and Parker, but not those of Nivala *et al.* [15]. A more comprehensive analysis will require the inclusion of recovery kinetics in order to extend the model to the regime when the wave nucleation time is short.

A second limitation of our study is that we have not explored the role of site-to-site heterogeneities. Experimental observations [24] of Ca wave nucleation in astrocytes reveal

that Ca waves originate at repetitive sites which are strongly correlated with regions of the cell with high protein expression, and also with the presence of mitochondria. These results suggest that heterogeneities within cells are substantial and play a crucial role in determining nucleation sites. Also, experimental studies have shown that the distribution of RyR clusters in cardiac myocytes is broadly distributed [25]. This result indicates that clusters with a much larger than average number of channels could potentially drive the initiation of SCR. To include heterogeneities it will be necessary to include site disorder in our stochastic simulation and mean-field theory. In this case we expect wave nucleation to still occur at the localization sites of the leading eigenvector of Q_{ij} [Eq. (8)]. These localization sites will be determined by both the distribution of site disorder and the spatial arrangement of release sites. Hence, while our simplified approach neglects some key factors, it allows us to study the interplay between fluctuations and geometry in the nucleation of Ca waves. Further refinement of these ideas will be necessary to make more direct contact with experiments.

VI. CONCLUSION

In this study we have introduced a simplified model of Ca activity in a cardiac cell. Using this model we identify the region in parameter space where the spatial arrangement of CRUs dictates the sites of wave nucleation. In this regime we show that wave nucleation occurs at localized regions determined by the eigenvectors of the connectivity matrix. These results serve as a starting point to understand the interplay between fluctuations and geometry in the formation of Ca waves.

ACKNOWLEDGMENTS

This work was supported by the National Heart, Lung, and Blood Institute Grant No. RO1HL101196. E.A.-L. acknowledges funding from the Secretaría de Estado de Investigación, Desarrollo e Innovación (Spain), under Grant No. FIS2011-28820-C02-01.

[1] M. D. Bootman and M. J. Berridge, Cell **83**, 675 (1995).
[2] D. M. Bers, Nature (London) **415**, 198 (2002).
[3] H. Cheng and W. J. Lederer, Physiol. Rev. **88**, 1491 (2008).
[4] L. T. Izu, W. G. Wier, and C. W. Balke, Biophys. J. **80**, 103 (2001).
[5] T. Takamatsu and W. G. Wier, FASEB J. **4**, 1519 (1990).
[6] W. Chen, G. Aistrup, J. A. Wasserstrom, and Y. Shiferaw, Am. J. Physiol: Heart Circulatory Physiol. **300**, H1794 (2011).
[7] E. G. Lakatta, M. C. Capogrossi, A. A. Kort, and M. D. Stern, Fed. Proc. **44**, 2977 (1985).
[8] R. P. Katra and K. R. Laurita, Circulation Res. **96**, 535 (2005).
[9] W. Chen, M. Asfaw, and Y. Shiferaw, Biophys. J. **102**, 461 (2012).
[10] R. F. Gilmour, Jr. and N. S. Moise, J. Am. Coll. Cardiol. **27**, 1526 (1996).
[11] K. R. Laurita and R. P. Katra, J. Cardiovasc. Electrophysiol. **16**, 418 (2005).
[12] M. Bar, M. Falcke, H. Levine, and L. S. Tsimring, Phys. Rev. Lett. **84**, 5664 (2000).
[13] M. Falcke, L. Tsimring, and H. Levine, Phys. Rev. E **62**, 2636 (2000).
[14] M. Nivala, P. Korge, M. Nivala, J. N. Weiss, and Z. Qu, Biophys. J. **101**, 2102 (2011).
[15] M. Nivala, C. Y. Ko, M. Nivala, J. N. Weiss, and Z. Qu, J. Physiol. **591**, 5305 (2013).
[16] M. Nivala, C. Y. Ko, M. Nivala, J. N. Weiss, and Z. Qu, Biophys. J. **102**, 2433 (2012).
[17] J. S. Marchant and I. Parker, EMBO J. **20**, 65 (2001).
[18] C. Franzini-Armstrong, F. Protasi, and V. Ramesh, Biophys. J. **77**, 1528 (1999).
[19] C. Franzini-Armstrong, F. Protasi, and P. Tijskens, Ann. N. Y. Acad. Sci. **1047**, 76 (2005).
[20] M. Fill and J. A. Copello, Physiol. Rev. **82**, 893 (2002).
[21] M. Naraghi and E. Neher, J. Neurosci. **17**, 6961 (1997).
[22] M. Falcke and D. Malchow, *Understanding Calcium Dynamics: Experiments and Theory,* Lecture Notes in Physics No. 623 (Springer, Berlin, 2003)
[23] J. A. Hertz and K. H. Fischer, *Spin Glasses* (Cambridge University Press, Cambridge, 1991).
[24] P. B. Simpson, S. Mehotra, G. D. Lange, and J. T. Russell, J. Biol. Chem. **272**, 22654 (1997).
[25] D. Baddeley, I. D. Jayasinghe, L. Lam, S. Rossberger, M. B. Cannell, and C. Soeller, Proc. Natl. Acad. Sci. USA **106**, 22275 (2009).